Fig. S1

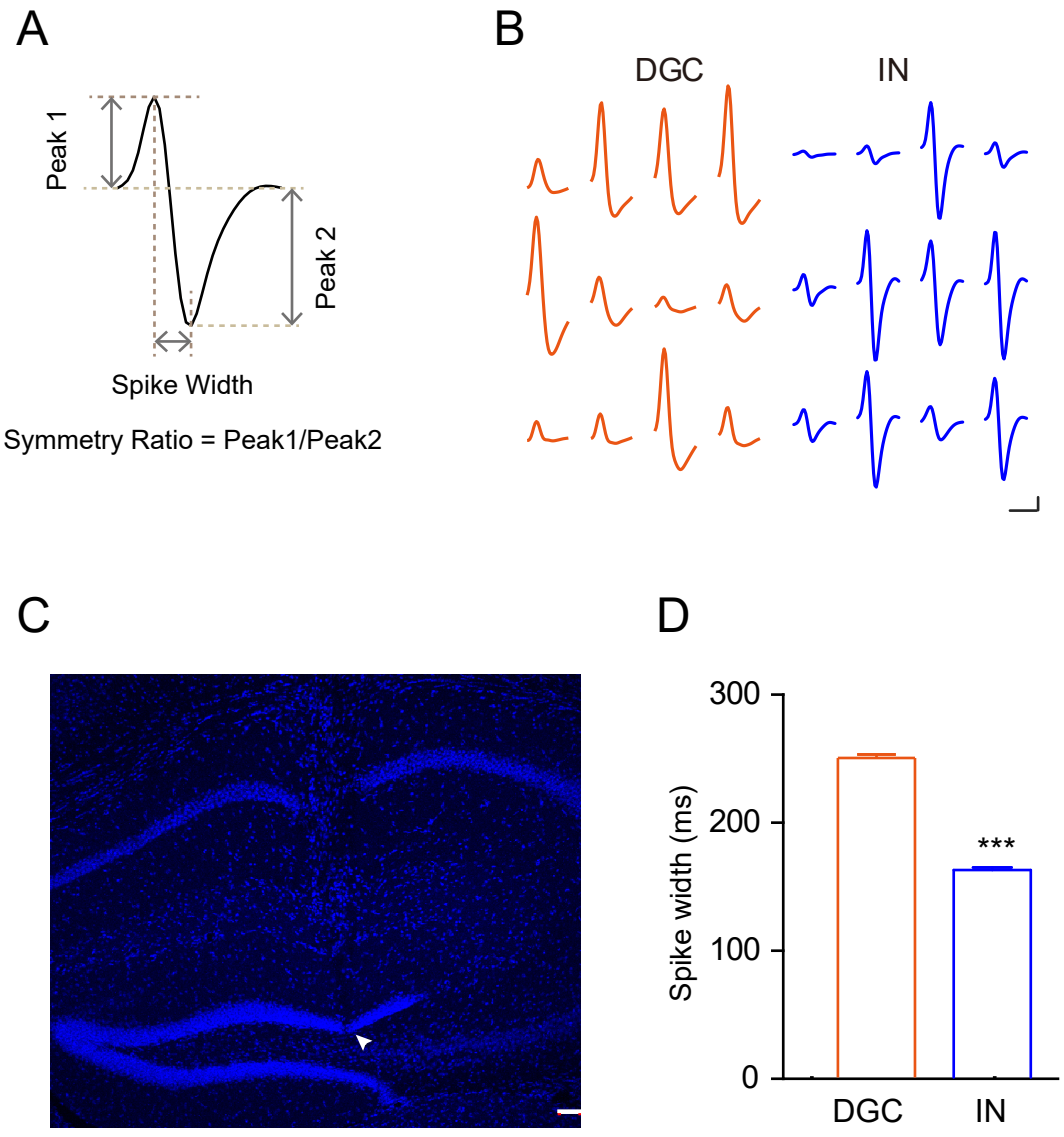

Supplementary Figure 1. Classification of recorded units in the dentate gyrus. A) Definition of symmetry and spike width of spike waveforms. **B)** Representative waveforms recorded from four channels of each tetrode classified as a putative interneuron (IN) or DGC. Scale bar: 5 mV and 10 ms. **C)** Representative coronal brain section showing the tetrode track of implantation (white arrow). Scale bar, 50 µm. **D)** Average spike width for DGCs and INs classified by principal component analysis using the parameters of symmetry ratio, long-term firing rate, and spike width (***p < 0.001; RM-ANOVA).

Fig. S2

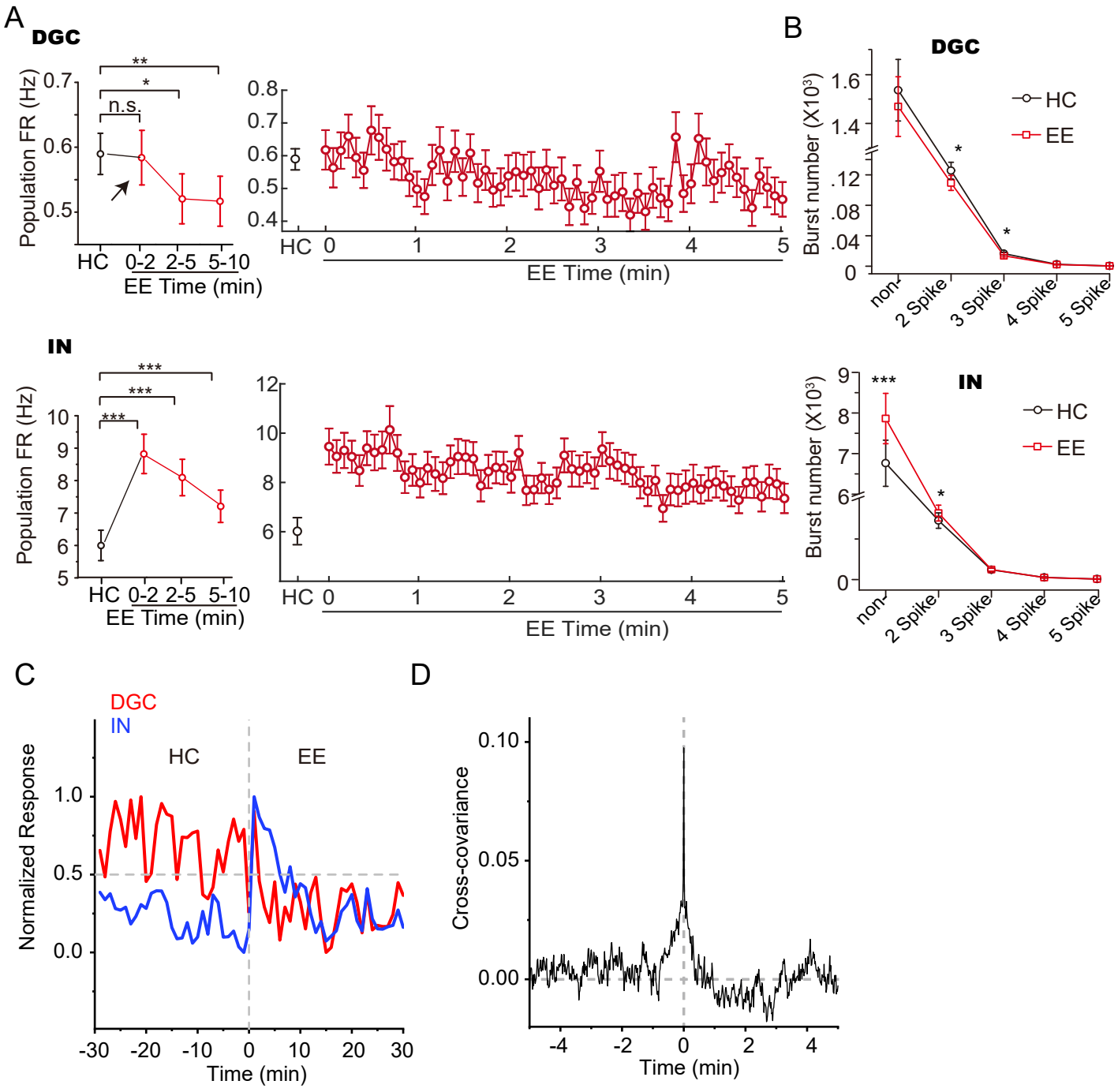

Supplementary Figure 2. Exploration enhances interneuron activity and suppresses DGC activity in the dentate gyrus. A) Average firing rate (FR) of DGCs (Top) and interneurons (INs; Bottom) during 30-min of HC recording and short-term EE recording (n.s., $p > 0.05$; *$p < 0.05$; **$p < 0.01$; ***$p < 0.001$; one-way RM-ANOVA). The FR of DGCs in the EE condition gradually decreased after 2 min compared with that in the HC condition. The FR of INs increased immediately after placement in the EE condition. **B)** Bursting and non-bursting activity of DGCs (left) and INs (right) in HC and EE conditions. Bursting was determined by counting the spikes with intervals < 10 ms. The number of spikes in one burst was calculated, and burst firings were grouped based on spike number. Non-burst firing indicates regular tonic firing. **C)**, Normalized firing rate of DGC and interneurons recorded from HC- and EE-sessions. **D)**, Averaged cross-covariance of DGC and interneuron firing under EE condition. The cross-covariance of DGC and interneuron firing was calculated basing on data from same day recording.

Fig. S3

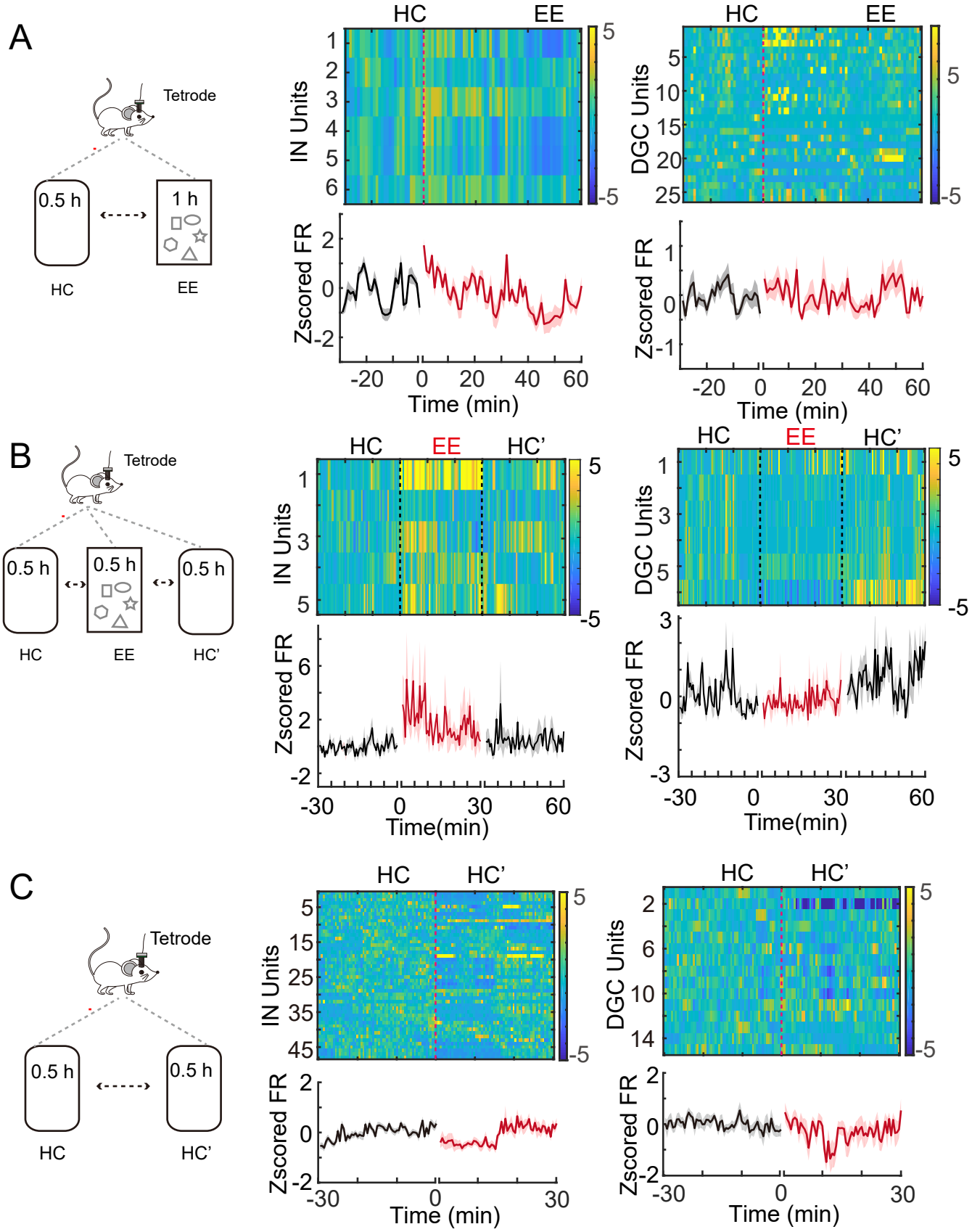

Supplementary Figure 3. Neuronal response to extended EE and return to HC. A) DGC and interneuron (IN) activity during 30 min in the HC condition and 1 h in the EE condition. Z-scored firing rate (FR) heatmaps (top) and average z-score value (bottom) showed that the increase of IN activity declined with longer exploration time. **B)** DGC and IN activity in the HC, EE, and return to HC conditions. Each session was 30 min. The increased IN activity and decreased DGC activity in the EE condition returned to baseline levels after return to the HC condition. **C)** Effect of transfer of mice from one familiar environment (HC) to another familiar environment (HC') on the FR of DGCs and INs. In contrast to the increased FR seen in the HC-to-EE transition, the HC-to-HC' transition induced a slight decrease in IN activity, with no substantial changes observed for DGCs.

Fig. S4

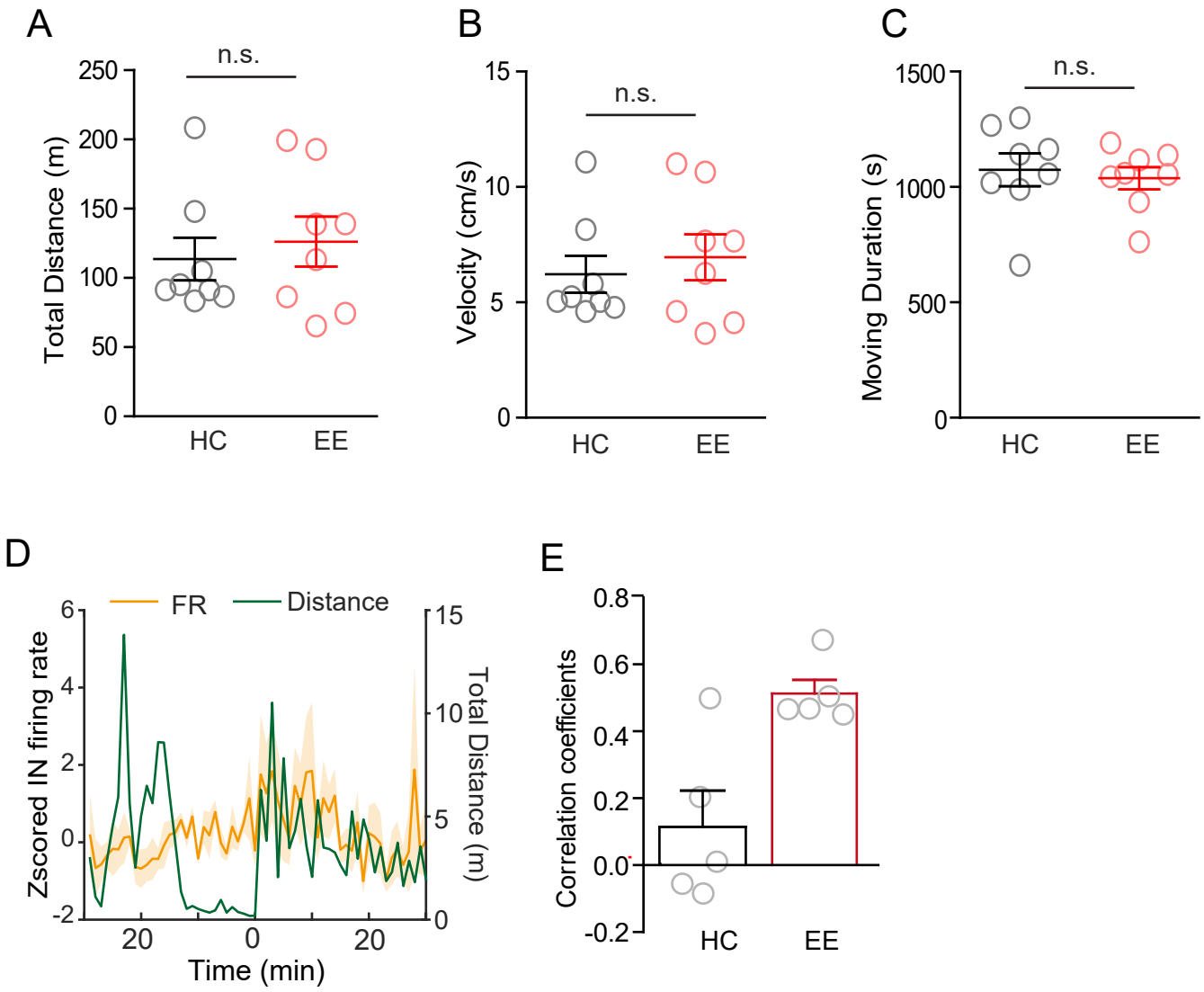

Supplementary Figure 4. Exploration activities of free-moving recording animals. A-C) Averaged moving distance (A), velocity (B) and moving duration (C) from each recording showing no significant difference between HC -and EE-recording. n.s., $p > 0.05$, unpaired student t-test. **D)** Representative trace of averaged interneuron firing rate (n= 4) and mouse locomotion from one recording as the function of recording time. **E)** Correlation coefficient analysis showing firing activity of five interneurons have a significant correlation to locomotion activity.

Fig. S5

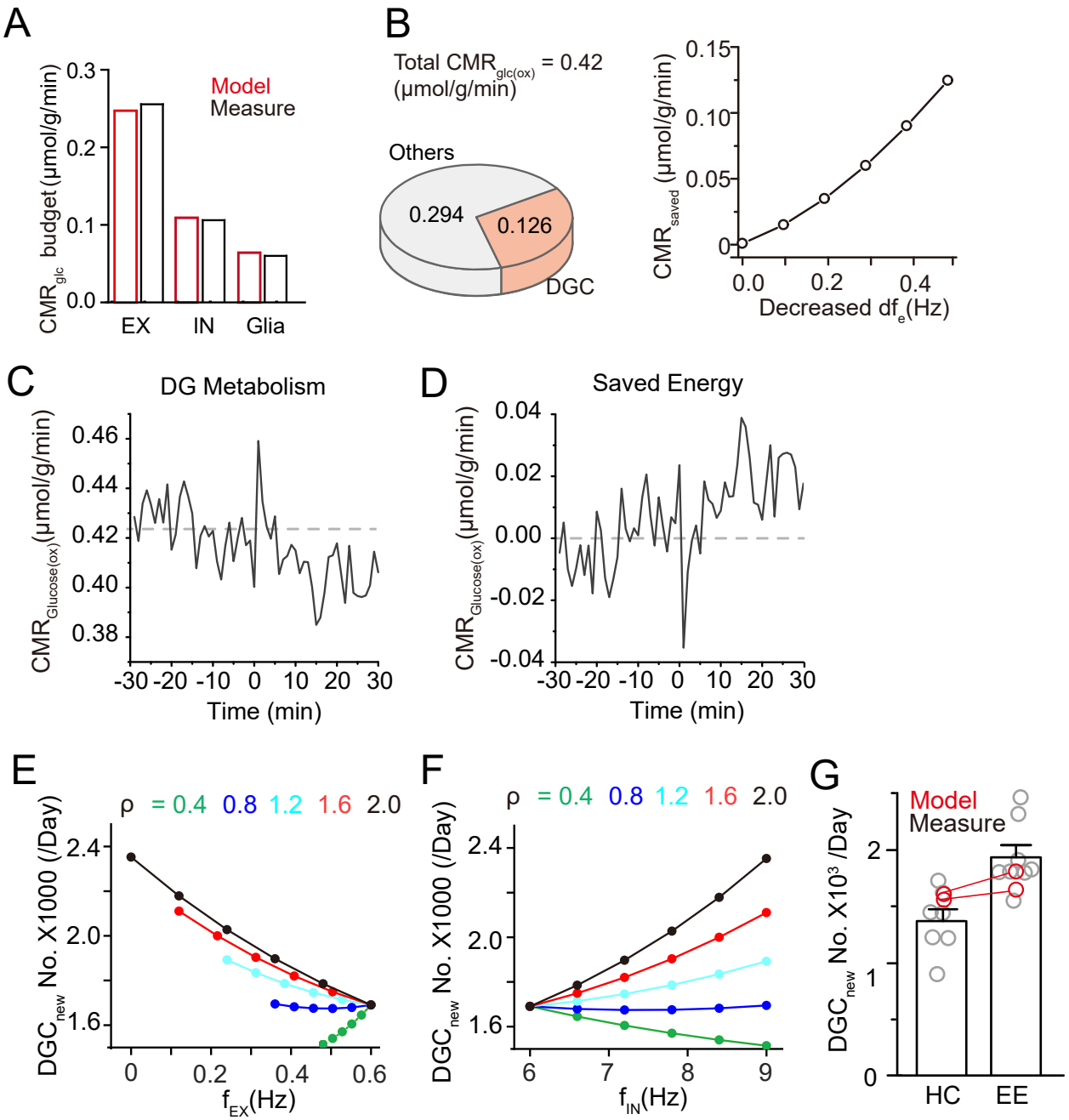

Supplementary Figure 5. Energy budget links the activity and survival of newborn neurons. A) Validation of the model by comparing calculated energy budget with measured metabolism for excitatory cells (EX), inhibitory cells (INT), and glia. Experimental data were adapted from previous studies (Patel, Tiwari, Veeraiah, & Saba, 2018; Saba et al., 2017). **B)** Left, allocated energy for DGCs calculated based on the energy budget model. Right, relationship of saved energy for newborn neurons and change of circut activity. The circuit activity was represented as a function of net DGC firing rate. **C-D)** Base on the circuit activity, predicated dynamics of energy consumption (C) and saved energy (D) across the HC- and EE-conditions. **E)** Relationship between EX activity and number of surviving newborn neurons. **F)** Relationship between INT activity and number of surviving newborn neurons. **G)** Measured (gray) and predicted (red) number of newborn neurons every day. Neurogenesis was calculated based on circuit activities of individual animal via mathematic model.

Fig. S6

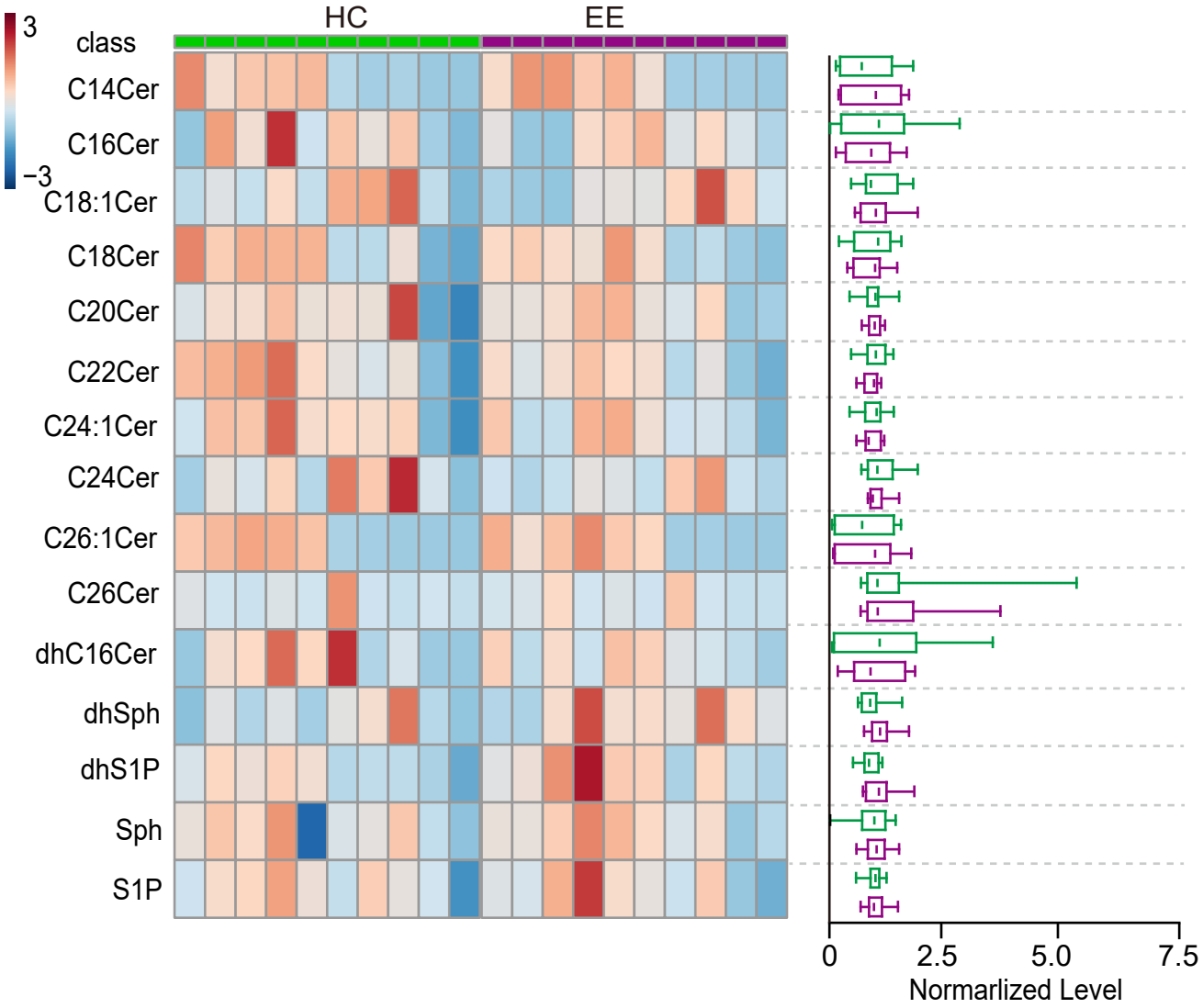

Supplementary Figure 6 Lipidomics of cortex tissue of HC and EE mice Lipidomic analysis of cortex tissue from home cage and enriched environment treatment mice. The EE- cortex have a similar level of ceremide and sphingosine lipids with HC-cortex. HC, n = 10; EE, n = 10, unpaired T- test.

Fig. S7

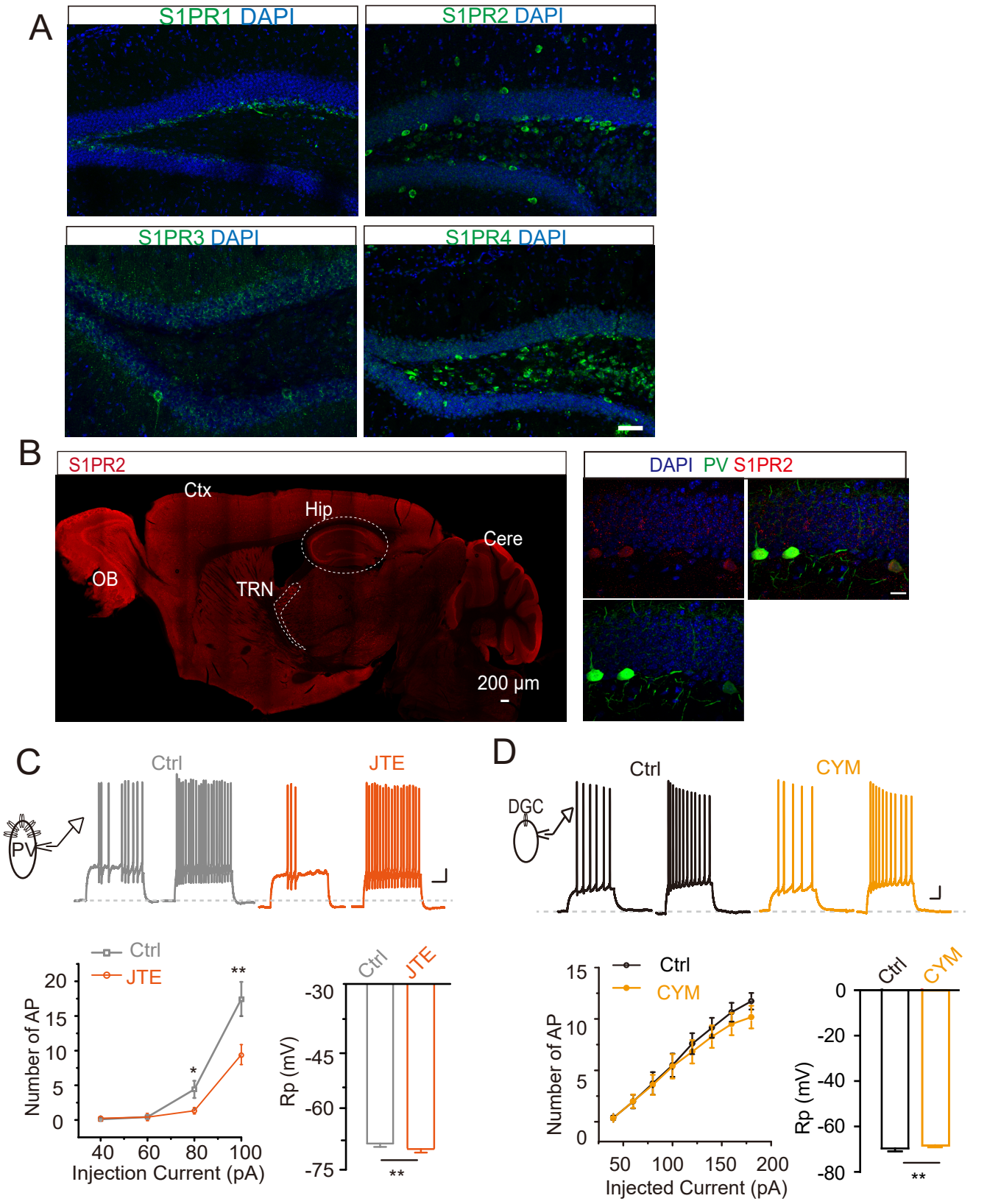

Supplementary Figure 7. Distribution of S1P receptors and the regulation of S1PR2 on dentate gyrus neurons. A) Distribution of SP1 receptors 1–4 in the dentate gyrus. S1PR1 was enriched in cells in the subgranular zone. S1PR2 was highly expressed by some cells with a sparse distribution. S1PR3 was heavily located in neuronal dendrites, and S1PR4 was mostly present in cells in the hilus. **B)** Representative images showing whole-brain S1PR2 expression (left, scale bar: 200 μm) and S1PR2 expressed in PV-positive neurons (right, scale bar: 10 μm). **C)** Blockade of S1PR2 by its antagonist JTE-013 (JTE, 25 μM) decreased PV-positive interneuron activity as indicated by the suppression of current-evoked action potentials (APs) and hyperpolarization of the resting membrane potential (Rp). **D)** Activation of S1PR2 by using CYM5520 (CYM, 10 μM) had no significant effect on APs and a slight depolarizing effect on Rp. *p < 0.05; **p < 0.01, repeated-measures ANOVA.

Fig. S8

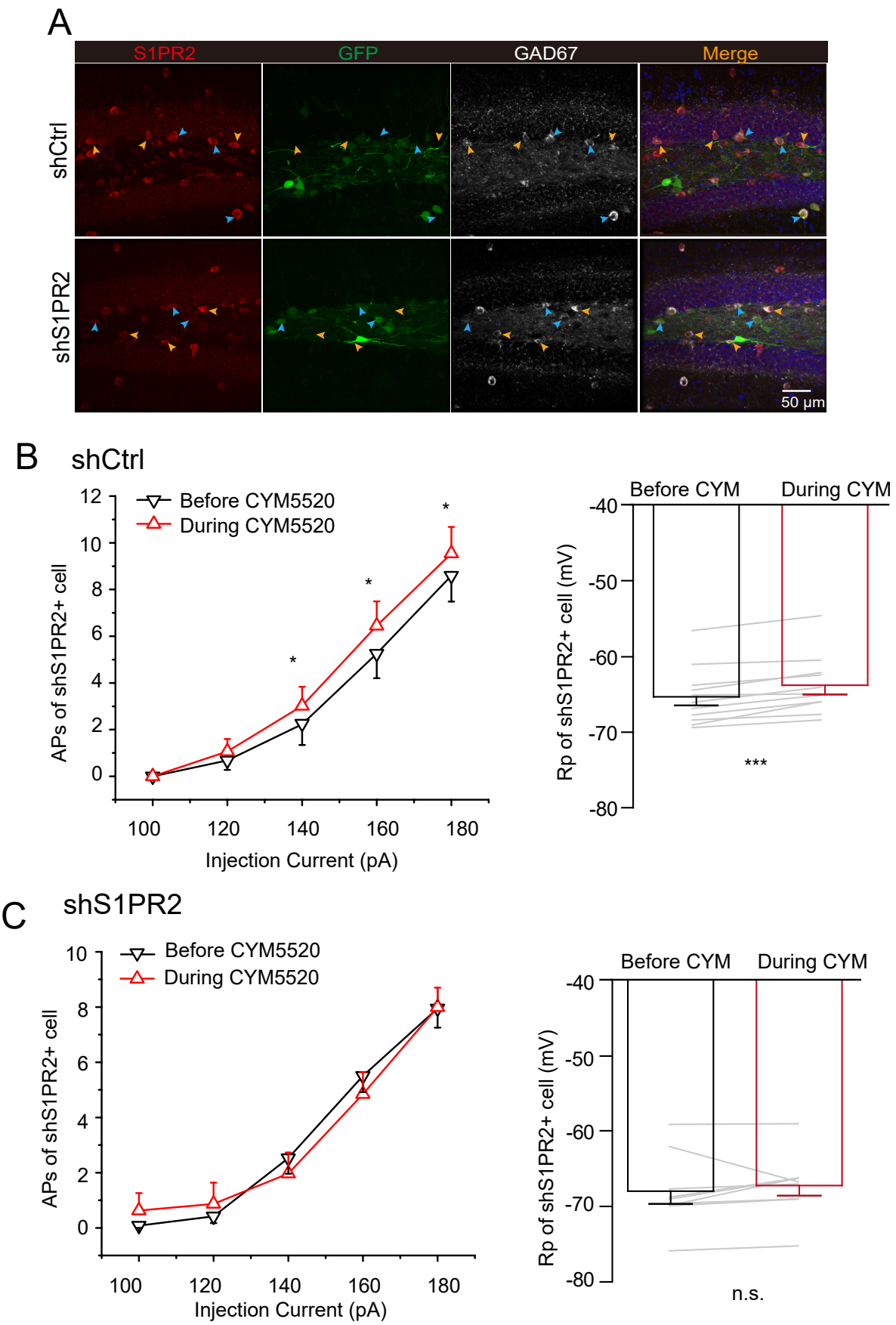

Supplementary Figure 8. Validation of S1PR2 knock down in the dentate gyrus. A) GFP-tagged AAV9-mediated expression of shS1PR2 or shCtrl in the dentate gyrus. Interneurons uninfected or infected by virus are indicated by yellow or blue arrows, respectively. **B–C)** Number of current-evoked action potentials (APs) and resting membrane potential (Rp) with or without application of the S1PR2 agonist CYM5520 (10 µM) (shCtrl, n = 12 **(B)**; shS1PR2 n =11 (**C**); n.s., $p > 0.05$; *$p < 0.05$, ***$p < 0.001$; paired t-test).

Fig. S9

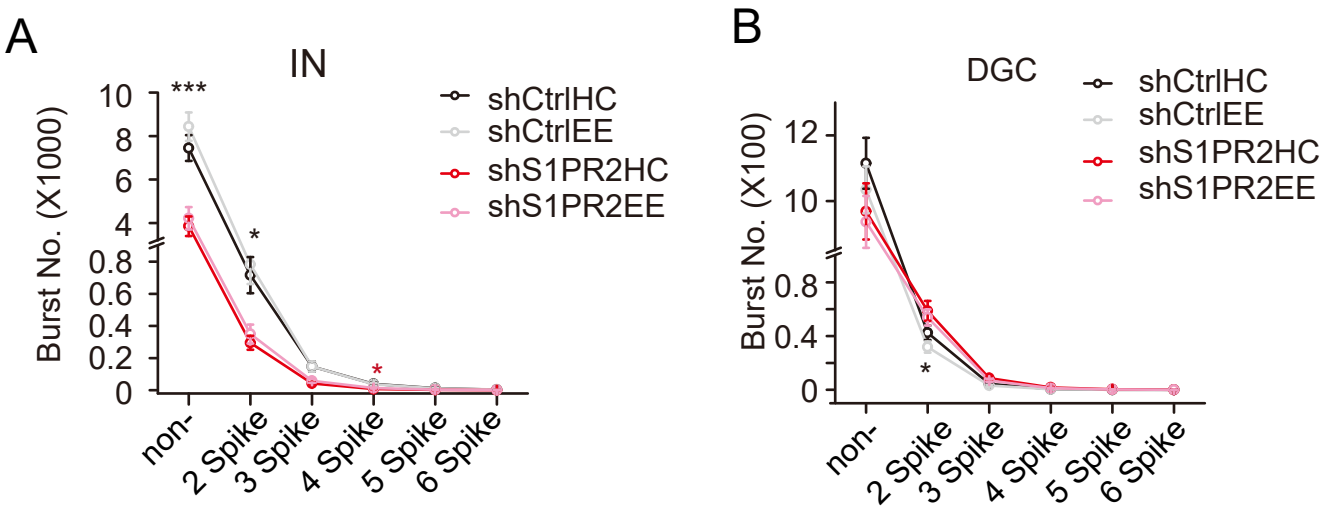

Supplementary Figure 9. Burst and non-burst firing in the control and S1PR2 knock-down dentate gyrus. A) The average number of non-burst and burst firings of interneurons (INs) in the shCtrl group increased in the EE condition compared with the HC condition. Knock down of S1PR2 suppressed the EE-induced increase in non-burst and burst firing. **B)** The average number of non-burst and burst firings of DGCs in the shCtrl and shS1PR2 groups. Bursting was determined by counting the spikes with intervals < 10 ms. The number of spikes in one burst was calculated, and burst firings were grouped based on spike number. Non-burst firing indicates regular tonic firing. *p < 0.05; ***p < 0.001, one-way RM-ANOVA.

Fig. S10

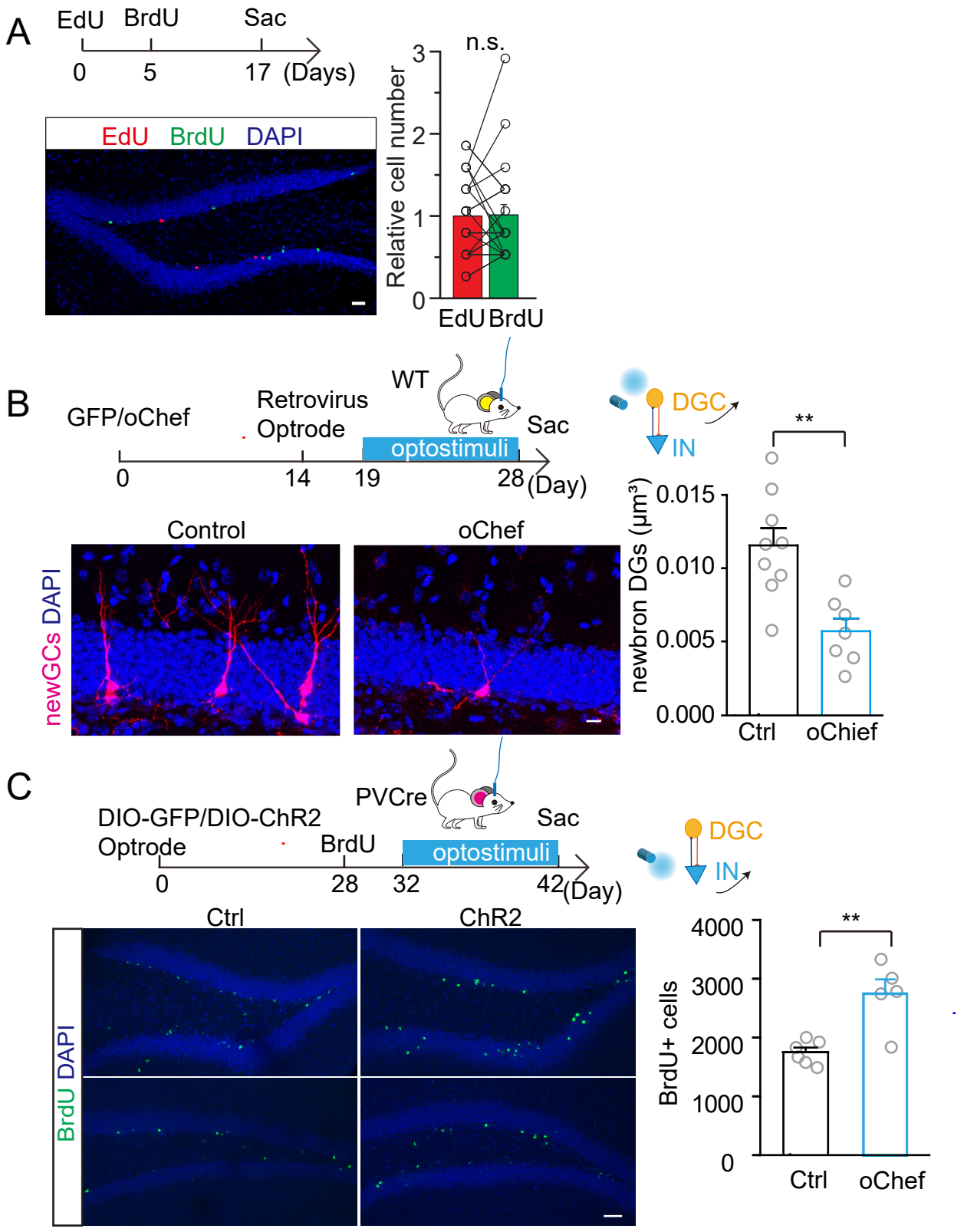

Supplementary Figure10. Neural activity in the dentate gyrus regulates hippocampal neurogenesis. A) Two pulses of proliferating neurons were labeled using EdU and BrdU. The number of surviving newborn DGCs was similar between pulses, suggesting that their survival rate remains constant under a given condition. Scale bar, 50 μm. **B)** GFP-tagged AAV-CaMKII-mediated expression of oChef in DGCs. Control mice were injected with AAV expressing GPF only. Newborn neurons were labeled by retrovirus with a tdTomato reporter. Activation of mature DGCs reduced the survival of newborn neurons. Scale bar, 10 μm. **C)** GFP-tagged AAV-DIO-mediated expression of oChef in PV-positive interneurons in PV-Cre mice. Newborn neurons were labeled by one-time BrdU injection. Activation of PV-positive interneurons increased the survival of newborn neurons. Scale bar, 50 μm. n.s., $p > 0.05$, **$p < 0.01$, unpaired t-test.

Fig. S11

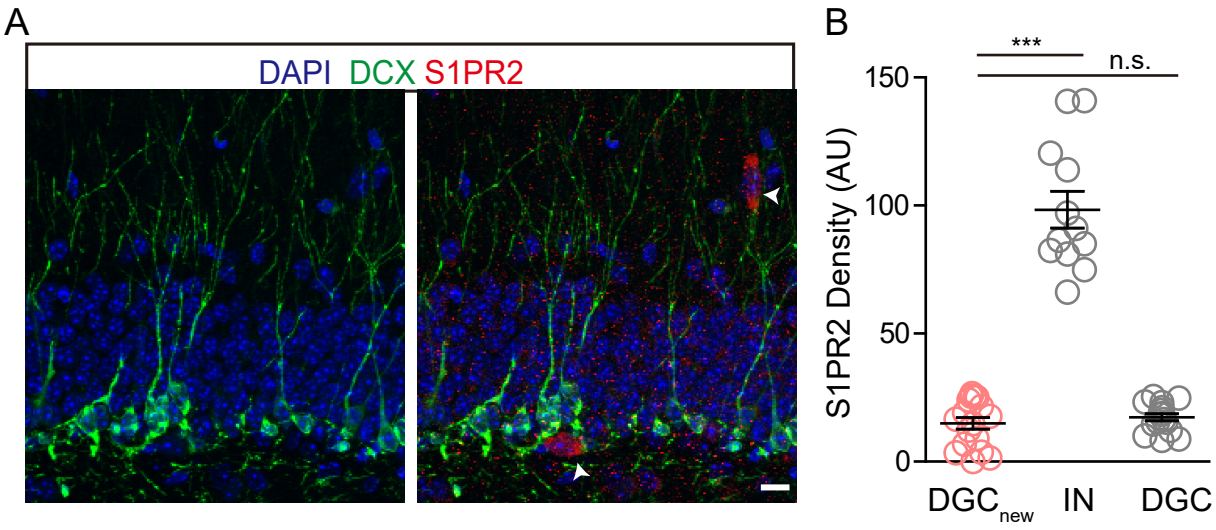

Supplementary Figure 11. Expression of S1PR2 on immature neurons. A) Expression of S1PR2 on the subgranular zone where immature newborn DGC located. DCX signal was used to labelling the immature neurons. White arrows indicated two interneurons with dense S1PR2 signal. **B**) The expression level of S1PR2 in the newborn DGC cells is similar as in mature DGC but significantly lower than the interneurons. n.s., $p > 0.05$, ***$p < 0.001$, unpaired student t-test

Supplementary Video legends

Supplementary Video 1: A video clip showing the exploration activity of free-moving mouse in the home cage. Behavior activities were tracked and analyzed by using EthoVision XT (Noldus).

Supplementary Video 2: A video clip showing the exploration activity of free-moving mouse in the enriched environment. Behavior activities were tracked and analyzed by using EthoVision XT (Noldus).

Supplementary Methods

Whole-cell patch-clamp recording in acute brain slices

Brain slices from adult mice (2-4 months old) were prepared as previously described (1). Briefly, mice were deeply anesthetized with urethane and transcardially perfused with ice-cold N-methyl-D-glucamine artificial cerebrospinal fluid (NMDG ACSF) containing (in mM): 93 NMDG, 2.5 KCl, 1.2 NaH_2PO_4, 30 $NaHCO_3$, 20 N-2-hydroxyethylpiperaxine-N-2-ethanesulfonic acid (HEPES), 25 D-glucose, 2 thiourea, 5 Na-ascorbate, 3 Na-pyruvate, 0.5 $CaCl_2$, and 10 $MgSO_4$. The pH of NMDG ACSF was adjusted to 7.3–7.4 with concentrated HCl. Whole brains were rapidly removed from skulls and cut into 280-μm coronal slices using a vibratome (HM650V, Thermo Scientific) in ice-cold NMDG ACSF. Three to four slices containing the dorsal hippocampus were transferred into 34°C NMDG ACSF for 12 min and then transferred into room temperature HEPES ACSF for further incubation. HEPES ACSF contained (in mM): 92 NaCl, 2.5 KCl, 1.2 NaH_2PO_4, 30 $NaHCO_3$, 20 HEPES, 25 D-glucose, 2 thiourea, 5 Na-ascorbate, 3 Na-pyruvate, 2 $CaCl_2$, and 2 $MgSO_4$.

After more than 1 h of incubation, slices were transferred to a recording chamber for electrophysiological recording. The chamber was continuously perfused with 32°C oxygenated recording ACSF containing (in mM): 129 NaCl, 3 KCl, 1.2 KH_2PO_4, 1.3 $MgSO_4$, 20 $NaHCO_3$, 2.4 $CaCl_2$, 3 HEPES, and 10 D-glucose. Neurons in the DG were viewed with a 40× water-immersion objective in an upright microscope equipped with an interference contrast and fluorescence illumination (Zeiss). Patch pipettes were pulled from borosilicate capillaries using a horizontal P9 puller (Narishige, Tokyo, Japan). For whole-cell patch-clamp recording, we used a HEKA EPC-10 amplifier and PatchMaster software (HEKA Electronics, Lambrecht (Pfalz), Germany) for data acquisition. Signals were filtered at 2.9 kHz and digitized at 10 kHz. The resistance of the recording pipettes was 4–6 MΩ when filled with K-gluconate intracellular solution and 2.5–4.5 when filled with K-Cl intracellular solution. K-gluconate solution contained (in mM): 130 K-gluconate, 2 $MgCl_2$, 5 KCl, 0.6 EGTA, 10 HEPES, 2 Mg-ATP, and 0.3 Na-GTP. K-Cl solution contained (in mM): 120 KCl, 30 NaCl, 5 EGTA, 10 HEPES, 1 $MgCl_2$, 0.5 $CaCl_2$, and 2 Mg-ATP. The osmolarity of the intracellular solutions was adjusted to 285-290 mOsm/kg, and pH was adjusted to 7.2 by KOH (1 M) solution. The liquid junction potential was calculated at ~15 mV and was not corrected in the final quantification. Recordings were made at least 3 min after establishing a whole-cell configuration under stable conditions in both voltage- and current-clamp modes. Data were discarded if the series resistance changed by > 20% of its initial value during voltage-clamp recording. Data analysis was performed and figures generated using Clampfit 10.0 (Axon) and Origin (Originlab). Drugs used for whole-cell patch clamping were dissolved in ultrapure water or 10% DMSO as stock solutions at 1,000 times final concentration. PhotoS1P was dissolved in recording ACSF at a concentration of 2 mM/L and stocked at -20°C before use. Before perfusion and activation of PhotoS1P by 473-nm wavelength illumination (1 mW, LED, Thorlabs), PhotoS1P was maintained in the dark for longer than 20 min (2).

Immunostaining and quantification

Mice were deeply anesthetized with urethane (250 μg/g) and perfused transcardially with phosphate-buffered saline (PBS) followed by 4% fresh

paraformaldehyde (PFA) in PBS. Whole brains were dissected, kept in 4% PFA overnight, and transferred into 30% (w/v) sucrose in PBS. After sinking, brains were sectioned into 40–50 µm coronal slices for immunostaining. Sections were first permeabilized with 0.5% Triton X-100 in PBS (PBST) for 20 min and then blocked with 10% donkey serum dissolved in 0.25% PBST for 1 h at room temperature. Sections were incubated with primary antibodies for S1PR2 (rabbit polyclonal antibody, 1:250, NOVUS), BrdU (rat monoclonal antibody, 1:500, Abcam), GAD67 (mouse monoclonal antibody, 1:500, Millipore), DCX (goat polyclonal antibody, 1:250, Santa Cruz), or NeuN (mouse monoclonal antibody, 1:500, Millipore) in 0.25% PBST overnight with shaking at 4°C. Finally, sections were switched to secondary Alexa 488-conjugated donkey anti-mouse antibody (1:1,000, Invitrogen), Alexa 488-conjugated donkey anti-rat antibody (1:1,000, Invitrogen), Alexa 564-conjugated donkey anti-rabbit antibody (1:1,000, Jackson Immuno Research), Alexa 647-conjugated donkey anti-goat antibody (1:1,000, Jackson Immuno Research), or Alexa-647 conjugated donkey anti-rabbit antibody (1:1,000, Jackson Immuno Research) for 3 h with shaking at room temperature.

For BrdU and EdU staining, sections were permeabilized in 4% PBST for 1 h followed by a first reaction for EdU-alkyne and a second reaction with cold azide. Each reaction was 15 min at room temperature. The buffer for EdU-alkyne was 10 µM Alexa 555-conjugated azide, 20 mM sodium ascorbate, and 4 mM copper sulfate in PBS. The buffer for cold azide was 2 mM azidomethylphenylsulfide, 20 mM sodium ascorbate, and 4 mM copper sulfate in PBS. After three washes in PBS, sections were HCl-denatured for 25 min at 37°C and neutralized by 0.1 M borate at pH 8.0 for 20 min at room temperature, followed by blocking with 5% donkey serum for 1 h at room temperature. Sections were incubated in primary anti-rat BrdU antibody (1:500) overnight and Alexa 488-conjugated donkey anti-rat antibody for 3 h at room temperature. Images were obtained using an Olympus FLV1000 or Zeiss confocal microscope. For BrdU counting, we performed immunostaining in every fourth brain section across the entire anterior-posterior axis of the hippocampus. BrdU positive cells within the granular cell layer and subgranular zone of DG were counted for further analysis. We then multiplied the counted number from both hemispheres by four to match the total number of labeled cells, as we described previously (3, 4). Fluorescence intensity was quantified using ImageJ software. The average voxel intensity of fluorescence was acquired through region of interest analysis.

Metabolomics profiling

Twelve C57BL/6 (8-week-old) male mice were evenly divided into HC and EE groups. Mice in the EE group was kept in an enriched environment with 4–6 novel objects replaced every day, whereas mice in the HC were kept in their home cage. All mice were anesthetized with urethane and transcardially perfused with ice-cold PBS buffer. Hippocampi from both hemispheres were separated immediately and stored in a -80°C freezer until processing. For sample extraction, several recovery standards were used prior to the first step in the extraction process to allow confirmation of extraction efficiency (MicroLab STAR system, Hamilton Company). To remove protein, dissociate small molecules bound to protein or trapped in the precipitated protein matrix, and recover chemically diverse metabolites, samples were precipitated with methanol for 2 min (Glen Mills GenoGrinder 2000) followed by centrifugation. Samples were placed briefly on a

TurboVap (Zymark) to remove the organic solvent content and then frozen and dried under nitrogen. Instrument variability was determined by calculating the median relative standard deviation for the standards added to each sample prior to injection into the mass spectrometers. Overall process variability was determined by calculating the median relative standard deviation for all endogenous metabolites (i.e., non-instrument standards) present in 100% of the pooled matrix samples. Metabolomic profiling analysis utilized multiple platforms, including ultra-high performance liquid chromatography/tandem mass spectrometry (UPLC-MS/MS) methods and hydrophilic interaction chromatography (HILIC)/UPLC-MS/MS, which was performed by Metabolon, Inc. Aliquots of sample were analyzed using a Waters Acquity UPLC (Waters Corp.) and LTQ mass spectrometer (MS) (Thermo Fisher Scientific, Inc.), which consisted of an electrospray ionization source and linear ion-trap mass analyzer. The MS analysis alternated between MS and data-dependent MSn scans using dynamic exclusion; scanning varied slightly between methods but covered 70–1,000 mass-to-charge ratio.

A global metabolite covering classes including amino acids, carbohydrates, lipids, nucleotides, microbiota metabolism, energy, cofactors and vitamins, xenobiotics, and novel metabolites was investigated. Compounds were identified by comparison to library entries for purified standards, including retention time/index, mass-to-charge ratio, and chromatographic data (including MS/MS spectral data) using Metabolon's hardware and software. Peaks were quantified using area under the curve. Each raw concentration of metabolite was rescaled to set the median equal to 1, and missing values were imputed with the minimum. Comprehensive metabolomic data analysis was performed using MetaboAnalyst 4.0 (https://www.metaboanalyst.ca) (5). Unsupervised principal component analysis was applied for preliminary evaluation of data quality for HC and EE groups. Hierarchical cluster analysis (based on t-tests) was performed to create a heatmap of differentially expressed metabolites using MetaboAnalyst 4.0. To identify significantly different metabolic pathways between groups, all metabolites were analyzed using MetaboLync Pathway Visualizations (Metabolon, Inc).

Lipidomics analysis

For lipidomics analysis, mice (8-week-old) were placed in HC or EE conditions for 1 h, after which they were anesthetized with urethane and transcardially perfused with ice-cold Tris-HCL (pH 7.4, 20 mM). Hippocampi from both hemispheres were combined into a single sample. The somatosensory cortex of some mice was also collected. All samples were homogenized with 0.2 mL Tris-HCL and protease/phosphatase inhibitor (Cell Signaling) using an electronic homogenizer (Precellys 24, Bertin). Homogenates were sonicated for two cycles of 30 s with a 10-s interval. After centrifuging, the supernatant of the samples was added to 2 mL extraction buffer (2:3, 70% isopropanol:ethyl acetate) and stored at -80°C before lipid profiling. The protein concentration of all samples was measured using bicinchoninic acid assay (BCA). Lipid extraction and mass spectrometry were performed as previously described (6). Briefly, 50 µL internal standards were added prior to lipid extraction. The supernatant of the resuspended sample was transferred into a glass tube, and 2 mL extraction buffer was added. Extracts were dried using a nitrogen dryer and resuspended in 150 µL mobile phase buffer (100% methanol with 1 mM ammonium acetate and 0.2% formic acid). For mass spectrometry analysis, stocked extracts were separated on a Thermo TSQ

Quantiva-triple quadrupole with uHPLC. Results of MS analysis wasnormalized to total protein.

Method References

1. Y. Jin *et al.*, Sodium salicylate suppresses GABAergic inhibitory activity in neurons of rodent dorsal raphe nucleus. *PLoS One* **10**, e0126956 (2015).
2. J. Morstein *et al.*, Optical control of sphingosine-1-phosphate formation and function. *Nat Chem Biol* **15**, 623-631 (2019).
3. J. Shen *et al.*, Neurovascular Coupling in the Dentate Gyrus Regulates Adult Hippocampal Neurogenesis. *Neuron* 10.1016/j.neuron.2019.05.045 (2019).
4. G. W. Kirschen *et al.*, Active Dentate Granule Cells Encode Experience to Promote the Addition of Adult-Born Hippocampal Neurons. *J Neurosci* **37**, 4661-4678 (2017).
5. J. Chong *et al.*, MetaboAnalyst 4.0: towards more transparent and integrative metabolomics analysis. *Nucleic Acids Res* **46**, W486-W494 (2018).
6. J. Bielawski, Z. M. Szulc, Y. A. Hannun, A. Bielawska, Simultaneous quantitative analysis of bioactive sphingolipids by high-performance liquid chromatography-tandem mass spectrometry. *Methods* **39**, 82-91 (2006).

Supplementary-document-for-model

Mathematical model to compute hippocampal neurogenesis in the adult brain

Goal: To examine how the alteration of neural circuit activity impacts hippocampal neurogenesis, we computed the relationship between neural circuit activity and hippocampal neurogenesis based on energy consumption redistribution.

Procedures for establishing the mathematical model

Overview: We employed energy homeostasis and redistribution among different cell types in the hippocampus to establish a mathematical model. We first established equations to calculate the energy consumption of each type of cell in the dentate gyrus (DG) of the adult mouse brain. We validated these parameters by comparing the calculated energy consumption of cells with experimental data from positron-emission tomography measurement (1). As the firing of excitatory and inhibitory neurons is the key factor influencing energy consumption in the DG, we established a general mathematical model to compute the number of surviving newborn dentate granule cells (DGCs) per day using firing rate as an input. We validated this model by comparing its predicted neurogenesis rate with experimental data, which showed similar numbers of newborn neurons. Below are the three major steps used to build the model:

Step 1. Compute the energy consumption of cells in the DG of the adult mouse brain

Overview: The energy budget for each type of cell (active DGC, aE_{DGC}; silent DGC, sE_{DGC}; newborn DGC, E_{DGC0}; mossy cell, E_{MC}; interneuron, E_{IN}; astrocyte, E_{AC}; oligodendrocyte, E_{OD}; microglial cell, E_{MG}) was calculated as below:

$$
\begin{aligned}
aE_{DGC} &= E_{HK}^{DGC} + E_{RP}^{DGC} + (E_{AP}^{DGC} + E_{ST}^{DGC} + E_{glu}^{DGC} + E_{Ca}^{DGC}) f_e = a_1 + b_1 f_e \\
sE_{DGC} &= E_{HK}^{DGC} + E_{RP}^{DGC} + (E_{AP}^{DGC} + E_{ST}^{DGC} + E_{glu}^{DGC} + E_{Ca}^{DGC}) f_e / 10 = a_1 + 0.1 b_1 f_e \\
E_{DGC0} &= a_1 + 0.1 b_1 f_e \\
E_{MC} &= E_{HK}^{MC} + E_{RP}^{MC} + f_e (E_{AP}^{MC} + E_{ST}^{MC} + E_{glu}^{MC} + E_{Ca}^{MC}) = a_2 + b_2 f_e \\
E_{IN} &= E_{HK}^{IN} + E_{RP}^{IN} + f_i (E_{AP}^{IN} + E_{ST}^{IN} + E_{GABA}^{IN} + E_{Ca}^{IN}) = a_3 + b_3 f_i \\
E_{AC} &= E_{HK}^{AC} + E_{RP}^{AC} + f_e E_{Ca}^{AC} = a_4 + b_4 f_e \\
E_{OD} &= E_{HK}^{OD} + E_{RP}^{OD} + f_e E_{Ca}^{OD} = a_5 + b_5 f_e \\
E_{MG} &= E_{HK}^{MG} + E_{RP}^{MG} + f_e E_{Ca}^{MG} = a_6 + b_6 f_e
\end{aligned}
$$

(S1)

E_{HK}, E_{RP}, E_{AP}, E_{ST}, E_{glu}, and E_{Ca} represent the energy budget for housekeeping, maintenance of membrane resting potential, action potentials, synaptic transmission, glutamate or GABA metabolism, and presynaptic calcium entry into neurons, respectively. To simplify these equations, a_x (= E_{HK} + E_{RP}) with x (= 1, 2, …) represented the summation of constant parameters (i.e., costs of housekeeping and maintenance of resting potential), and b_x (= E_{AP} + E_{ST} + E_{glu} + E_{Ca}) represented the summation of varying parameters (i.e., action potentials, synaptic transmission, recycling of transmitters, and calcium transport for neurons; calcium

entry for glial cells). Note that for DGC energy budget calculation, we separated DGCs into an active DGC (aDGC) group with an average firing rate of f_e and a silent GC (sDGC) group with a firing rate of $f_e/10$. Experimental studies show that ~3% DGCs are active (2, 3), whereas 97% are generally inactive. The values of a_x and b_x are presented in STable 1. Note that the terms f_e and f_i represent the firing rates of excitatory and inhibitory neurons, respectively.

The following sections provide the details of calculating E_{HK}, E_{RP}, E_{AP}, E_{ST}, E_{glu}, and E_{Ca} for each type of cell in the DG.

1) Cellular housekeeping (E_{HK})

Housekeeping energy for neurons is the basal metabolic energy that supports basal functions associated with biosynthesis (e.g., protein and lipid synthesis, cytoskeletal rearrangement). The energy for this cellular housekeeping (E_{HK}) is about 10-15% of the total energy cost of a neuron and is proportional to the cellular mass (4). Therefore, we began to calculate E_{HK} by incorporating the mass of different cell types. For simplicity, we assumed all glial cells have an equal mass (m_g) and that all neurons have an equal mass (m_n). We used the following cell body diameters to measure cellular mass: 17 μm for mossy cells, 15 μm for DGCs and interneurons, and 10 μm for glial cells. Based on the total number of each type of cell and the mass of the DG (6.79 mg), we established a formula as:

$$M_{DG} = N_{DGC} * mDGC + N_{glia} \times m_{glia} + N_{Mossy} \times m_{Mossy} \quad \text{(S2)}$$

The total mass is calculated as 9.956×10^{-9} g for mossy cells, 6.8394×10^{-9} g for both interneurons and DGCs, and 2.027×10^{-9} g for glial cells. Based on previous measurements, the metabolic rate of glial cells is about 0.06 μmol/g/min glucose oxidation (5, 6), with which we calculated a glia rate in DG is 1.3734×10^{14} ATP/s. The total glial cell number in the DG is around 412,794(7), and the individual glial cost is around 3.327×10^{8} ATP/s. Given that E_{HK} requires ~25% of the total glial cell metabolic consumption (1, 8), the housekeeping metabolic rate for an individual glial cell is $E_{HK} = 8.2 \times 10^{-7}$ ATP/sec. Based on the scaling law (4) between the metabolic rate and mass value, calculated E_{HK} values are listed in STable 1.

2) Maintaining resting potential (E_{RP})

Neurons and glial cells require energy to maintain their resting membrane potential due to the leakiness of the cell membrane to ions. Based on previous studies (8), we calculated the energy required for resting potential maintenance (E_{RP}) as follows:

$$E_{RP} = (V_{Na} - V_{RP}) \times (V_{RP} - V_K) / [F\, R_m(V_{RP} + V_{Na} - 3V_K)] \quad \text{(S3)}$$

where E_{RP} has a unit of ATP/sec, and F is the Faraday constant. V_{Na}, V_K, and V_{RP} represent the Nernst potentials for Na^+, K^+, and the resting membrane potential, respectively. Based on previous studies, we used the Nernst potentials V_{Na} = -50 mV and V_K = -100 mV for all types of cells (1, 8). For cell-type specific resting membrane potentials, we used following: V_{RP} = -80 mV for DGCs, -60 mV for newborn DGCs (9-11), -70 mV for mossy cells (12, 13), -65 mV for GABAergic interneurons (14, 15), -80 mV for astrocytes (16, 17), -40 mV for microglia (18), and -70 mV for oligodendrocytes (17). R_m is the input resistance of the cell membrane (230 MΩ for

DGCs (10, 14), 150 MΩ for mossy cells (12, 13), 3 GΩ for newborn DGCs (9-11), 220 MΩ for GABAergic interneurons (14, 15), 560 MΩ for astrocytes (17), 3.9 GΩ for microglia (18), and 100 MΩ for oligodendrocytes (17)). Calculated E_{RP} values are listed in STable 1.

3) Cost of action potential conduction (E_{AP})

Action potential conduction along neuronal axons and dendrites induces an influx of Na^+, which requires substantial energy for subsequent efflux for ion homeostasis (i.e., 1 ATP energy corresponding to 3 Na^+). Hence, the energy for action potential conduction (E_{AP}) in individual neurons was calculated as:

$$E_{AP} = f \Delta Q_{Na} / 3 \quad \text{(S4)}$$

where f is the average neuronal firing rate, and ΔQ_{Na} is the total Na^+ charge transmitted during action potential conduction. In line with methods used in recent reports (1, 8), the minimum amount of Na^+ influx needed to charge the membrane to depolarize to the peak of an action potential is $\Delta Q_{min} = S C_m \Delta V$, where S is the membrane surface area, C_m is the membrane capacitance, and ΔV is the amplitude of the action potential measured from the spike threshold to the peak. The actual Na^+ charge is always larger than the theoretical minimum Na^+ influx because Na^+ influx and K^+ efflux occur simultaneously. Thus, in the calculation $\Delta Q_{Na} = \varepsilon \Delta Q_{min} = \varepsilon S C_m \Delta V$, ε is the overlap ratio of Na^+ influx to K^+ efflux. The membrane surface area S of a neuron was calculated as:

$$S = S_{axon} + S_{dend} + S_{soma} \quad \text{(S5)}$$

where ε is ~1.5 for cortical axons in pyramidal cells and 2.2 for interneurons. The membrane surface area S of the axon is calculated as $S_{axon} = \pi d_{axon} L_{axon}$. Here, the axon diameter (d_{axon}) is 0.3 μm for all neuron types, with an axon length (L_{axon}) of 2.88 mm for DGCs, and interneurons and 4 mm for mossy cells. Dendrite diameter (d_{dend}) is 0.7 μm for all neuron types, and dendrite length (L_{dend}) is 0.32 mm for DGCs and interneurons and 0.44 mm for mossy cells. Soma diameter is 15 μm for DGCs and interneurons and 17 μm for mossy cells. Calculated E_{AP} values are listed in STable 1.

4) Cost of synaptic transmission (E_{ST}^{gm})

We used the same methods described by previous reports (1, 8) to calculate presynaptic and postsynaptic cost for neurons (i.e., ion influx through ionotropic receptors) as:

$$E_{ST} = f \rho_{ves} n_{bouton} E_{ves} \quad \text{(S6)}$$

where f is the average firing rate of a neuron, ρ_{ves} is the vesicle neurotransmitter release probability, with a value believed to decrease exponentially with an increasing value of f (e.g., 0.7 for ~0.1 Hz firing rate, 0.64 for ~1 Hz firing rate, and 0.45 for ~4 Hz firing rate at 37°C) (8, 19). The release probability versus glutamatergic firing rate can be described by the fitting equation $\rho_{ves} = 0.6 \exp(-f/10.6) + 0.128$), where f is the firing rate (0.6 Hz for DGCs and 6 Hz for interneurons), n_{bouton} is the number of boutons in a presynaptic terminal (5,760 for DGCs and 8,000 for mossy cells and GABAergic neurons), and E_{ves} is the energy cost for releasing

one vesicle of neurotransmitters. E_{ves} is 1.64×10^5 ATP molecules (8). Calculated energy costs for synaptic transmission are listed in STable 1.

5) Cost of neurotransmitter recycling (E^e_{glu} and E^i_{GABA})

Previous reports show that 3.67 ATP molecules are required to recycle each glutamate molecule (1). This calculation leads to a total $E_{recycling}$ of 14,680 ATP molecules for 4,000 glutamate molecules (1). For each glutamatergic neuron, the total cost for glutamate recycling in DGCs and mossy cells was calculated as:

$$E^e_{glu} = f \; r_{ves} \; n_{bouton} \; E_{recycling} \quad \text{(S7)}$$

where f is the firing rate, ρ_{ves} is the vesicle neurotransmitter release probability, and n_{bouton} is the number of presynaptic terminals. Similarly, for each GABAergic neuron, the total cost for GABA recycling in interneurons was described as:

$$E^i_{GABA} = f \; r_{ves} \; n_{bouton} \; E_{recycling} \quad \text{(S8)}$$

Calculated energy costs for neurotransmitter recycling are listed in STable 1.

6) Cost of calcium entry (E_{Ca})

Action potentials trigger calcium influx ($E_{Ca} = 1.2 \times 10^4$ calcium per vesicle) in the presynaptic terminals of neurons. For ionic homeostasis, it costs 1.2×10^4 ATPs for the membrane to expel calcium for each vesicle that is released (i.e., 1 ATP molecule corresponding to 1 Ca^{2+} ion) (8). Hence, the total cost for calcium entry for individual neurons was calculated as:

$$E_{Ca} = f \; r_{ves} \; n_{bouton} \; E_{Ca} \quad \text{(S9)}$$

Glial cells, such as astrocytes, also have significant active calcium responses accompanying spiking activation of neurons. Neuronal activity-dependent transmitter release raises calcium influx in astrocytes by activating metabotropic glutamate receptors. Calcium transients in astrocytes are recorded in over half of neuronal calcium responses and are associated with transient arterial vasodilation (20, 21). Hence, for glial cells in the DG, the energy costs needed to include active calcium signaling responses can be expressed as E_{Ca} (glial) = γE_{Ca} (DGC), with γ ranging from 0 to 1, but we assumed an optimized value of 0.8 to fit the experimental data. Calculated energy costs for calcium entry are listed in STable 1.

STable 1. Energy budget for all components of each cell type in the DG.

Cell Type	**Cell Component**	**Calculated budget for 1 Hz spike rate** (*Unit:* $\times 10^8$ *ATP/s*)	**Calculated budget for f_e and f_i** (*Unit:* $\times 10^8$ *ATP/s*)	**Calculated $a_x = E_{HK} + E_{RP}$ $b_x = E_{AP} + E_{ST} + E_{glu} + E_{Ca}$**	**Cell calculated budget** (*Unit:* $\times 10^8$ *ATP/s*)
	E_{HK}	1.835	1.835		
	E_{RP}	2.204	2.20	$a_1 = 4.039$	

Active DGC (f_e = 0.6 Hz)	E_{AP}	0.685	0.411	b_1 = 8.318	9.03
	E_{ST}	6.565	3.939		
	E_{glu}	0.588	0.288		
	E_{Ca}	0.48	0.353		
Silent DGC (f_e = 0.06 Hz)	E_{HK}	1.835	1.835	a_1 = 4.039 b_1 = 8.318	4.538
	E_{RP}	2.204	2.20		
	E_{AP}	0.685	0.041		
	E_{ST}	6.565	0.394		
	E_{glu}	0.588	0.0288		
	E_{Ca}	0.48	0.0353		
MC (f_e = 0.6 Hz)	E_{HK}	2.357	2.357	a_2 = 6.895 b_2 = 11.55	13.825
	E_{RP}	4.538	4.54		
	E_{AP}	0.95	0.57		
	E_{ST}	9.117	5.47		
	E_{glu}	0.816	0.40		
	E_{Ca}	0.667	0.49		
Newborn DGC (f_e = 0.06 Hz)	E_{HK}	1.835	1.835	a_1 = 4.039 b_1 = 8.318	4.538
	E_{RP}	2.204	2.20		
	E_{AP}	0.685	0.041		
	E_{ST}	6.565	0.394		
	E_{glu}	0.588	0.0288		
	E_{Ca}	0.48	0.0353		
IN (f_i = 6 Hz)	E_{HK}	1.835	1.835	a_3 = 5.243 b_3 = 8.007	53.564
	E_{RP}	3.408	3.408		
	E_{AP}	0.904	5.426		
	E_{ST}	6.149	36.893		
	E_{glu}	0.504	2.699		
	E_{Ca}	0.45	3.302		
AC	E_{HK}	0.815	0.815	a_4 = 1.720 b_4 = 0.48	2.009
	E_{RP}	0.905	0.905		
	E_{Ca}	0.48	0.288		
OD	E_{HK}	0.815	0.815	a_5 = 7.625 b_5 = 0.48	7.911
	E_{RP}	6.81	0.681		
	E_{Ca}	0. 48	0.288		
MG	E_{HK}	0.815	0.815	a_6 = 1.055 b_6 = 0.647	1.3434
	E_{RP}	0.240	0.240		
	E_{Ca}	0. 647	0.40		

Step 2. Redistribute the cellular energy cost in the DG based on changes in neuronal firing rate

Overview: Based on the energy consumption calculated for each cell type, we modeled how energy redistribution occurs depending on changes in neuronal firing rate. To model the DG energy budget in this regard, we adapted physiological data and parameters reported in a recent detailed anatomical study of the mouse DG (volume 6.2 mm^3, mass 6.79 mg) (7) as follows: DGCs ($N_{DGC} = 6.12938 \times 10^5$), newborn DGCs ($N_{DGC0}$ =248,007), mossy cells (N_{MC} = 122,372), GABAergic interneurons (N_{IN} = 46,071), astrocytes (N_{AC} = 110,642), oligodendrocytes (N_{OD} = 124,165), and microglia (N_{MG} = 177,987). We expect that the numbers of most cell types in the adult brain do not change across the lifespan except for those of DGCs due to ongoing neurogenesis.

The total energy budget for the DG includes energy costs of excitatory cells (E_e), inhibitory cells (E_i), and glial cells (i.e., astrocytes, oligodendrocytes, and microglial cells; E_g) as follows:

$$E_{DG} = E_e + E_i + E_g \quad \text{(S10)}$$

E_e, E_i, and E_g were derived from:

$$\begin{aligned} E_e &= N_{DGC}E_{DGC} + N_{MC}E_{MC} + N_{DGC0}E_{DGC0} \\ E_i &= N_{IN}E_{IN} \\ E_g &= N_{AC}E_{AC} + N_{OD}E_{OD} + N_{MG}E_{MG} \end{aligned} \quad \text{(S11)}$$

E_{GC}, E_{MC}, E_{DGC0}, E_{IN}, E_{AC}, E_{OD}, and E_{MG} represent metabolic costs of individual DGCs, mossy cells, newborn DGCs, interneurons, astrocytes, oligodendrocytes, and microglial cells, respectively. Results of the present and previous studies indicate that that ~3% DGCs are active with average firing rates of ~0.6 Hz (Fig. 1F), whereas most (~97%) DGCs are less active with an average 0.06 Hz firing rate (22, 23). Therefore, as before, we separated DGCs into active (aDGC) group with an average firing rate f_e and silent (sDGC) group with an average rate $f_e/10$. Together, we calculated the energy budget for all DGCs as:

$$\begin{aligned} N_{DGC}E_{DGC} &= 3\% \times N_{DGC} \times aE_{DGC} + 97\% \times N_{DGC} \times sE_{DGC} \\ aE_{DGC} &= E_{HK}^{DGC} + E_{RP}^{DGC} + (E_{AP}^{DGC} + E_{ST}^{DGC} + E_{glu}^{DGC} + E_{Ca}^{DGC}) f_e = a_1 + b_1 f_e \\ sE_{DGC} &= E_{HK}^{DGC} + E_{RP}^{DGC} + (E_{AP}^{DGC} + E_{ST}^{DGC} + E_{glu}^{DGC} + E_{Ca}^{DGC}) f_e / 10 = a_1 + 0.1 b_1 f_e \end{aligned} \quad \text{(S12)}$$

where $a_1 = E_{HK}^{DGC} + E_{RP}^{DGC}$, $b_1 = E_{AP}^{DGC} + E_{ST}^{DGC} + E_{glu}^{DGC} + E_{Ca}^{DGC}$, and E_{HK}, E_{RP}, E_{AP}, E_{ST}, E_{glu}, and E_{Ca} represent the energy budget for cellular housekeeping, maintenance of membrane resting potential, action potential conduction, synaptic transmission, glutamate or GABA recycling, and presynaptic calcium entry into neurons, respectively. Note that f_e and f_i represent the firing rates of excitatory and inhibitory neurons, respectively. In the DG of the adult mouse brain, we found that f_e = 0.6 Hz and f_i = 6 Hz in experimental recordings. With these numbers, we simplified Eq. S12 to:

$$N_{DGC}E_{DGC} = N_{DGC}(a_1 + 0.127 b_1 f_e) \quad \text{(S13)}$$

To simplify the model, we considered newborn DGCs as silent DGCs (i.e., $E_{DGC0} = sE_{DGC}$ with N_{DGC0} = 248,007) because the newborn DGCs have a immature of synaptic transmission comparing with mature DGCs. Below is a summary of the calculation of the energy budget of all types of cells:

$$E_{DGC} = a_1 + 0.127 b_1 f_e \quad \text{(S14)}$$

$$
\begin{aligned}
&\mathrm{E}_{\mathrm{DGC0}} = a_1 + 0.1 b_1 f_e \\
&\mathrm{E}_{\mathrm{MC}} = \mathrm{E}_{\mathrm{HK}}^{\mathrm{MC}} + \mathrm{E}_{\mathrm{RP}}^{\mathrm{MC}} + f_e(\mathrm{E}_{\mathrm{AP}}^{\mathrm{MC}} + \mathrm{E}_{\mathrm{ST}}^{\mathrm{MC}} + \mathrm{E}_{\mathrm{glu}}^{\mathrm{MC}} + \mathrm{E}_{\mathrm{Ca}}^{\mathrm{MC}}) = a_2 + b_2 f_e \\
&\mathrm{E}_{\mathrm{IN}} = \mathrm{E}_{\mathrm{HK}}^{\mathrm{IN}} + \mathrm{E}_{\mathrm{RP}}^{\mathrm{IN}} + f_i(\mathrm{E}_{\mathrm{AP}}^{\mathrm{IN}} + \mathrm{E}_{\mathrm{ST}}^{\mathrm{IN}} + \mathrm{E}_{\mathrm{GABA}}^{\mathrm{IN}} + \mathrm{E}_{\mathrm{Ca}}^{\mathrm{IN}}) = a_3 + b_3 f_i \\
&\mathrm{E}_{\mathrm{AC}} = \mathrm{E}_{\mathrm{HK}}^{\mathrm{AC}} + \mathrm{E}_{\mathrm{RP}}^{\mathrm{AC}} + f_e \mathrm{E}_{\mathrm{Ca}}^{\mathrm{AC}} = a_4 + b_4 f_e \\
&\mathrm{E}_{\mathrm{OD}} = \mathrm{E}_{\mathrm{HK}}^{\mathrm{OD}} + \mathrm{E}_{\mathrm{RP}}^{\mathrm{OD}} + f_e \mathrm{E}_{\mathrm{Ca}}^{\mathrm{OD}} = a_5 + b_5 f_e \\
&\mathrm{E}_{\mathrm{MG}} = \mathrm{E}_{\mathrm{HK}}^{\mathrm{MG}} + \mathrm{E}_{\mathrm{RP}}^{\mathrm{MG}} + f_e \mathrm{E}_{\mathrm{Ca}}^{\mathrm{MG}} = a_6 + b_6 f_e
\end{aligned}
\tag{S1}
$$

In addition, the firing rates of mossy cells are less variable than those of DGCs, with a mean firing rate of 0.6 Hz based on experimental measurements and previous reports (23). Calculated values of a_x and b_x are shown in STable 1. Combining Eqs. S10, S11, and S12, we had:

$$
\begin{aligned}
&\mathrm{E}_{\mathrm{DG}} = \mathrm{N}_{\mathrm{DGC}}(a_1 + 0.127 b_1 f_e) + \mathrm{N}_{\mathrm{DGC0}}(a_1 + 0.1 b_1 f_e) + \mathrm{N}_{\mathrm{MC}}(a_2 + b_2 f_e) + \mathrm{N}_{\mathrm{IN}}(a_3 + b_3 f_i) \\
&+ \mathrm{N}_{\mathrm{AC}}(a_4 + b_4 f_e) + \mathrm{N}_{\mathrm{OD}}(a_5 + b_5 f_e) + \mathrm{N}_{\mathrm{MG}}(a_6 + b_6 f_e)
\end{aligned}
\tag{S15}
$$

which was further simplified as:

$$
\mathrm{E}_{\mathrm{DG}} = d_1 + d_2 f_e + d_3 f_i \tag{S16}
$$

where d_1, d_2, and d_3 are as constants, as we aimed to treat DGC and interneuron firing rates as variables. The constants were:

$$
\begin{aligned}
&d_1 = (\mathrm{N}_{\mathrm{DGC}} + \mathrm{N}_{\mathrm{DGC0}}) a_1 + \mathrm{N}_{\mathrm{MC}} a_2 + \mathrm{N}_{\mathrm{IN}} a_3 + \mathrm{N}_{\mathrm{AC}} a_4 + \mathrm{N}_{\mathrm{OD}} a_5 + \mathrm{N}_{\mathrm{MG}} a_6 \\
&d_2 = 0.127 b_1 \mathrm{N}_{\mathrm{DGC}} + 0.1 b_1 \mathrm{N}_{\mathrm{DGC0}} + \mathrm{N}_{\mathrm{MC}} b_2 + \mathrm{N}_{\mathrm{AC}} b_4 + \mathrm{N}_{\mathrm{OD}} b_5 + \mathrm{N}_{\mathrm{MG}} b_6 \\
&d_3 = \mathrm{N}_{\mathrm{IN}} b_3
\end{aligned}
\tag{S17}
$$

For adult mice, all parameters a_x and b_x in d_1, d_2, and d_3 were calculated as firing rate-independent constants (STable 1). The final calculated values were $d_1 = 5.887 \times 10^{14}$, $d_2 = 2.47 \times 10^{14}$, and $d_3 = 3.7103 \times 10^{13}$ (ATP/s), respectively. According to Eq. S16, we see that the DG budget can be altered by the excitatory activity rate f_e and inhibitory activity rate f_i.

A brief validation: Based on the above calculations, the total energy budget for the DG (E_{DG}) of an adult mouse is 9.6×10^{14} (ATP/s), which is equal to a 0.42 (μmol/g/min) glucose oxidation rate. All excitatory cells consume 5.6999×10^{14} ATP/s, all inhibitory cells consume 2.468×10^{14} ATP/s, and all glia consume 1.4436 × 1014 ATP/s, corresponding to 0.249, 0.108, and 0.063 (μmol/g/min) glucose oxidation rates, respectively. These results are consistent with experimental metabolic measurements (Fig. 2B) and measurements based on anatomical morphology and biophysical parameters of DGCs in previous studies. We note that, in converting the unit from ATP/s to a micromolar (6.02×10^{17} molecules) glucose oxidation per minute time for a gram unit mass of cortex tissue (μmol/g/min), we assumed that one molecule of glucose generally generates 33.6 ATP on average (assuming that glucose is not fully oxidized in the *in vivo* condition) (1, 24).

Step 3. Establish the relationship between excess energy and the number of newborn neurons in the DG

Overview: We next calculated whether changes in f_e and f_i parameters alter energy consumption in the DG, which may increase or decrease hippocampal neurogenesis (i.e., the number of newborn DGCs added to the existing DG circuit).

The above energy model was based on the DG of 1-year-old adult mice, presenting a DG metabolic budget of a ~0.42 (μmol/g/min) glucose oxidation rate. In this calculation, ~40% of the energy accounts for spiking activity and synaptic transmission, and ~60% accounts for housekeeping and maintenance of resting potential (Eq. S16 and S17). We expect that 0.42 is the amount of energy for the DG. We therefore examined how the excitation and inhibition firing rate alters the DG energy cost to possibly provide a surplus of energy for allocation to the neurogenesis process. We set the number of new DGCs (N_{GC}) as an unknown variable to be solved for by the equation derived from Eq. S15-17.

$$
\begin{aligned}
&\mathrm{E}_{\mathrm{DG}} = c_1 + c_2 f_e + c_3 f_i + \mathrm{N}_{\mathrm{DGC}}(a_1 + 0.127 b_1 f_e) \\
&c_1 = \mathrm{N}_{\mathrm{DGC0}} a_1 + \mathrm{N}_{\mathrm{MC}} a_2 + \mathrm{N}_{\mathrm{IN}} a_3 + \mathrm{N}_{\mathrm{AC}} a_4 + \mathrm{N}_{\mathrm{OD}} a_5 + \mathrm{N}_{\mathrm{MG}} a_6 \\
&c_2 = 0.1\mathrm{N}_{DGC0} b_1 + \mathrm{N}_{\mathrm{MC}} b_2 + \mathrm{N}_{\mathrm{AC}} b_4 + \mathrm{N}_{\mathrm{OD}} b_5 + \mathrm{N}_{\mathrm{MG}} b_6 \\
&c_3 = \mathrm{N}_{\mathrm{IN}} b_3 \\
&\mathrm{N}_{\mathrm{DGC}} = (\mathrm{E}_{\mathrm{DG}} - c_1 - c_2 f_e - c_3 f_i) / (a_1 + 0.127 b_1 f_e)
\end{aligned}
\qquad \text{(S18)}
$$

The N_{GC} generated in a 1-year period is determined by Eq. S18, which depends on f_e and f_i. The initial total number of DGCs in 3-month-old young adult mice was set as N_{DGC0} = 248,007.

As shown by experimental recordings, f_i directly modulates f_e based on the following equation:

$$
\begin{aligned}
f_i &= f_i^0 (1 + x) \\
f_e &= f_e^0 (1 - \rho x)
\end{aligned}
\qquad \text{(S19)}
$$

where f_i^0 and f_e^0 are the base firing rates of inhibitory and active excitatory DGCs. Here, f_e^0 = 0.6 Hz and f_i^0 = 6 Hz based on our experimental recordings from wild-type mice in the HC condition. For mice that were placed in the EE condition, the inhibitory neuronal firing rate could be increased by x%, which may suppress the excitatory neuronal firing rate by ρ*x*%, in which ρ is a variable. Due to interactions between inhibitory and excitatory neurons in the DG, the activity of DGCs depends on ρ, which we define as a constant factor in a given neural network. With different values of ρ, excitatory neurons show different responses to changes in interneuron activity.

Combining Eq. S18 and S19, we have:

$$
\begin{aligned}
&\mathrm{N}_{\mathrm{DGC}} = \frac{c_0 + (c_2 f_e^0 \rho - c_3 f_i^0) x}{a_1 + 0.127 b_1 f_e^0 (1 - \rho x)} \\
&c_0 = (\mathrm{E}_{\mathrm{DG}} - c_1 - c_2 f_e^0 - c_3 f_i^0)
\end{aligned}
\qquad \text{(S20)}
$$

Thus, the total number of surviving DGCs (N_{DGC}) in a 1-year lifespan can be predicted from the model Eq. S20. The average neurogenesis rate per day of DGCs was determined as:

$$R_{DGC}=N_{DGC}/365 \quad \text{(S21)}$$

R_{DGC} for different conditions of f_e and f_i as functions of x and ρ are shown in Fig. 2.

Supplementary References

1. Yu Y, Herman P, Rothman DL, Agarwal D, & Hyder F (2018) Evaluating the gray and white matter energy budgets of human brain function. *J Cereb Blood Flow Metab* 38(8):1339-1353.
2. Kee N, Teixeira CM, Wang AH, & Frankland PW (2007) Preferential incorporation of adult-generated granule cells into spatial memory networks in the dentate gyrus. *Nat Neurosci* 10(3):355-362.
3. Danielson NB*, et al.* (2016) Distinct Contribution of Adult-Born Hippocampal Granule Cells to Context Encoding. *Neuron* 90(1):101-112.
4. West GB, Brown JH, & Enquist BJ (1997) A general model for the origin of allometric scaling laws in biology. *Science* 276(5309):122-126.
5. Saba K*, et al.* (2017) Energetics of Excitatory and Inhibitory Neurotransmission in Aluminum Chloride Model of Alzheimer's Disease: Reversal of Behavioral and Metabolic Deficits by Rasa Sindoor. *Front Mol Neurosci* 10:323.
6. Patel AB, Tiwari V, Veeraiah P, & Saba K (2018) Increased astroglial activity and reduced neuronal function across brain in AbetaPP-PS1 mouse model of Alzheimer's disease. *J Cereb Blood Flow Metab* 38(7):1213-1226.
7. Ero C, Gewaltig MO, Keller D, & Markram H (2018) A Cell Atlas for the Mouse Brain. *Front Neuroinform* 12:84.
8. Attwell D & Laughlin SB (2001) An energy budget for signaling in the grey matter of the brain. *J Cereb Blood Flow Metab* 21(10):1133-1145.
9. Liu YB, Lio PA, Pasternak JF, & Trommer BL (1996) Developmental changes in membrane properties and postsynaptic currents of granule cells in rat dentate gyrus. *J Neurophysiol* 76(2):1074-1088.
10. Schmidt-Hieber C, Jonas P, & Bischofberger J (2004) Enhanced synaptic plasticity in newly generated granule cells of the adult hippocampus. *Nature* 429(6988):184-187.
11. Ambrogini P*, et al.* (2004) Morpho-functional characterization of neuronal cells at different stages of maturation in granule cell layer of adult rat dentate gyrus. *Brain Res* 1017(1-2):21-31.
12. Howard AL, Neu A, Morgan RJ, Echegoyen JC, & Soltesz I (2007) Opposing modifications in intrinsic currents and synaptic inputs in post-traumatic mossy cells: evidence for single-cell homeostasis in a hyperexcitable network. *J Neurophysiol* 97(3):2394-2409.
13. Scharfman HE & Schwartzkroin PA (1988) Electrophysiology of morphologically identified mossy cells of the dentate hilus recorded in guinea pig hippocampal slices. *J Neurosci* 8(10):3812-3821.
14. Mott DD, Li Q, Okazaki MM, Turner DA, & Lewis DV (1999) GABAB-Receptor-mediated currents in interneurons of the dentate-hilus border. *J Neurophysiol* 82(3):1438-1450.
15. Yuan M*, et al.* (2017) Somatostatin-positive interneurons in the dentate gyrus of mice provide local- and long-range septal synaptic inhibition. *Elife* 6.
16. McKhann GM, 2nd, D'Ambrosio R, & Janigro D (1997) Heterogeneity of astrocyte resting membrane potentials and intercellular coupling revealed by whole-cell and gramicidin-perforated patch recordings from cultured neocortical and hippocampal slice astrocytes. *J Neurosci* 17(18):6850-6863.
17. Harris JJ & Attwell D (2012) The energetics of CNS white matter. *J Neurosci* 32(1):356-371.
18. Schilling T & Eder C (2015) Microglial K(+) channel expression in young adult and aged mice. *Glia* 63(4):664-672.

19. Hardingham NR & Larkman AU (1998) Rapid report: the reliability of excitatory synaptic transmission in slices of rat visual cortex in vitro is temperature dependent. *J Physiol* 507 (Pt 1):249-256.
20. Schummers J, Yu H, & Sur M (2008) Tuned responses of astrocytes and their influence on hemodynamic signals in the visual cortex. *Science* 320(5883):1638-1643.
21. Belanger M, Allaman I, & Magistretti PJ (2011) Brain energy metabolism: focus on astrocyte-neuron metabolic cooperation. *Cell Metab* 14(6):724-738.
22. Neunuebel JP & Knierim JJ (2012) Spatial firing correlates of physiologically distinct cell types of the rat dentate gyrus. *J Neurosci* 32(11):3848-3858.
23. Senzai Y & Buzsaki G (2017) Physiological Properties and Behavioral Correlates of Hippocampal Granule Cells and Mossy Cells. *Neuron* 93(3):691-704 e695.
24. Hyder F*, et al.* (2016) Uniform distributions of glucose oxidation and oxygen extraction in gray matter of normal human brain: No evidence of regional differences of aerobic glycolysis. *J Cereb Blood Flow Metab* 36(5):903-916.